

# State selection in Taylor-vortex flow reached with an accelerated inner cylinder

By J. RIGOPOULOS, J. SHERIDAN AND M. C. THOMPSON

Department of Mechanical Engineering, Monash University, Clayton, Victoria 3800, Australia

(Received 20 May 2002 and in revised form 28 February 2003)

The selection of the axial wavelength in axisymmetric Taylor-vortex flow was studied by numerical experiments where the inner cylinder speed was linearly increased from subcritical to supercritical values over a finite ramp time to values not far above  $Re_c$ . For impulsive increases of the inner cylinder speed (zero ramp time) the preferred axial wavelength was less than the critical wavelength. As the ramp time was increased, the preferred axial wavelength increased and approached the critical wavelength, so that for very slow increases of the inner cylinder speed the preferred axial wavelength was equal to the critical wavelength. A linear model was developed which revealed that a linearly increased inner cylinder speed resulted in a delayed growth for each of the amplitudes of the modes. When the ramp time was sufficiently large, the amplitude of the mode with the critical wavelength was delayed the least from growing to high amplitudes. This mode then self-interacted and saturated resulting in steady Taylor-vortex flow. Finally, nonlinear effects and state selection are discussed from the point of view of nonlinear dynamics.

---

## 1. Introduction

In 1965 the seminal work of Coles established the non-uniqueness of Taylor-vortex flow at post-critical Reynolds numbers. He noted that for a given Reynolds number, approximately 20 or more different flow states could occur depending on the initial conditions and the way the final state was reached. The different final states were characterized by differing axial wavelengths and azimuthal wavenumbers. Since that time, that work has been extended (e.g. Snyder 1969; Burkhalter & Koschmieder 1973, 1974; Park, Gerald & Donnelly 1981; Andereck, Liu & Swinney 1986; Lim, Chew & Xiao 1998; Antonijoan & Sanchez 2002; Xiao, Lim & Chew 2002). In this paper, axisymmetric Taylor-vortex flow is the focus and the restricted case is considered where the outer cylinder is fixed. Experimentally, under these circumstances, non-uniqueness at the same final Reynolds number manifests itself as different numbers of Taylor vortices in a finite fluid column depending on parameters during the development stage. Hence, in this paper, the final state is identified with the axial wavelength of the Taylor vortices.

The diversity of possible flow states for cylindrical Taylor–Couette flow is indicated by the work of Andereck *et al.* (1986), and Andereck & Baxter (1988) who explored experimentally the rich variety of flows, depending on the inner and outer cylinder Reynolds numbers. They identified approximately 20 distinct flow types in the parameter space defined by these two Reynolds numbers.

For the case where the outer cylinder is stationary, the Reynolds number can be defined as  $Re = Vd/\nu$  where  $V$  is the inner cylinder speed,  $d$  is the gap size and  $\nu$

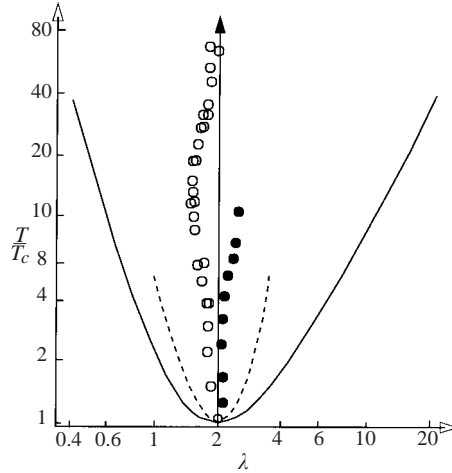


FIGURE 1. Stability diagram for Taylor-vortex flow for  $\eta = 0.727$ ,  $\mu = 0$ . Relative Taylor number ( $\mathcal{T}/\mathcal{T}_c = (Re/Re_c)^2$ ) versus axial wavelength. —, the neutral curve from the linear stability of steady circular Couette flow (Chandrasekhar 1961). - - -, the stability boundary from a weakly nonlinear analysis (Kogelman & Diprima 1970).  $\circ$ , Taylor-vortex flow states observed for sudden start experiments (Burkhalter & Koschmieder 1974).  $\bullet$ , Taylor-vortex flow states observed for an experiment where the annulus was filled with fluid after the inner cylinder was rotating at fixed speed. Reproduced from Burkhalter & Koschmieder (1974).

is the kinematic viscosity. The other important governing parameters are  $\eta = r_{in}/r_{out}$ , where  $r_{in}$  and  $r_{out}$  are the inner and outer radii; and  $\mu = \Omega_{out}/\Omega_{in}$ , where  $\Omega_{in}$  and  $\Omega_{out}$  are the inner and outer angular rotation rates. In addition, the aspect ratio,  $\Gamma$ , is the size of the axial domain relative to the gapsize. In this paper the ideal case is assumed, where the cylinders are assumed infinite in axial extent so that boundary effects can be ignored. For the numerical experiments described, a large periodic axial domain is chosen so that the computationally-allowed axial wavelengths are restricted as little as possible. More discussion of these points, and how the simulations relate to experimental results using different end conditions, is contained in § 6.

A well-known result of the linear stability analysis (Taylor 1923) is that there exists a minimum critical  $Re_{c,min}(=Re_c(\lambda_c))$ , at which one axial wavelength becomes linearly unstable. The situation is demonstrated in figure 1. The outer curve describes the variation of critical Reynolds number  $Re_c(\lambda)$  with axial wavelength of the axisymmetric perturbation. For a particular  $Re$  above a minimum critical value, there is a linearly unstable band of axial wavelengths. Infinitesimal axisymmetric perturbations with wavelengths in this band will grow exponentially. Outside the band, circular Couette flow is stable and infinitesimal axisymmetric perturbations decay exponentially.

However, stable Taylor-vortex flows have been achieved experimentally (Snyder 1969) for a much smaller band of wavelengths than the band derived from linear theory. A weakly nonlinear analysis by Kogelman & Diprima (1970) has shown that stable Taylor-vortex flows are achievable only for wavelengths within a band roughly  $1/\sqrt{3}$  times the width of the band from linear theory. The inner band (also shown in figure 1) is often called the Eckhaus stable band. The critical wavelength  $\lambda_c$  is defined as the wavelength corresponding to the minimum critical Reynolds number and takes the (dimensionless) value of 2.0 in figure 1.

Experiments by Burkhalter & Koschmieder (1973) have shown that when the inner cylinder speed is increased quasi-steadily from rest, the preferred axial wavelength

of the Taylor-vortex flow was equal to the critical wavelength,  $\lambda_c$ , and remained so for  $Re > Re_c$ . Burkhalter & Koschmieder (1974) also showed that when the inner cylinder speed is impulsively increased from rest the preferred axial wavelength,  $\lambda_s$ , is smaller than the critical wavelength. This is illustrated in figure 1, where data for impulsive increases are represented by the open circles. Stable Taylor-vortex flows with preferred wavelengths between  $\lambda_s$  and  $\lambda_c$  can be achieved by applying different inner cylinder acceleration rates to the same final Reynolds number (Koschmieder 1993). Thus, Taylor-vortex flows with different axial wavelengths within the Eckhaus stable range can be achieved depending on how the experiment is performed.

Lim *et al.* (1998) and Xiao *et al.* (2002) experimentally examined the effect of acceleration rate on the final state as the Reynolds number is linearly increased through the critical value from an initial to a final Reynolds number. They found that for an inner to outer cylinder radius ratio of  $\eta = 0.803$ , a second stationary Taylor-vortex flow regime with a much smaller wavelength occurred in a Reynolds number range where wavy Taylor-vortex flow was known to occur for quasi-steady increases. This new state occurred for acceleration rates greater than  $2.2 \text{ s}^{-1}$ . However, the existence of this regime was very sensitive to  $\eta$  and did not occur for either  $\eta = 0.660$  or  $\eta = 0.894$ . Antonijoan & Sanchez (2002) used stability analysis to determine the stability boundaries of wavy Taylor-vortex flow for the different azimuthal mode numbers as a function of Reynolds number and axial wavelength. They showed that for subcritical wavelengths there is a region of stability for Taylor-vortex flow surrounded by areas where wavy Taylor-vortex flow will occur. This only occurs for  $\eta$  above approximately 0.75. This provides a partial explanation for the results obtained by Lim *et al.* (1998) and Xiao *et al.* (2002).

This background leads to two fundamental questions about Taylor-vortex flow as posed by Koschmieder (1993). An explanation is needed as to why the wavelength of supercritical axisymmetric vortices is independent of the Taylor number and equal to the critical wavelength when the Taylor number is increased slowly from subcritical values. Also, why can supercritical axisymmetric vortices be non-unique.

To clarify the behaviour of the modes with different ramp times, Taylor-vortex flow was simulated numerically. This allowed us to study the independent growth and subsequent nonlinear interaction of many discrete axisymmetric modes.

## 2. Numerical method

The incompressible Navier–Stokes equations were written in cylindrical coordinates with radial ( $r$ ), azimuthal ( $\phi$ ) and axial ( $z$ ) components of velocity. Derivatives with respect to  $\phi$  were neglected owing to the assumption of axisymmetry. The resulting equations required the solution for the pressure  $P$  and the three components of velocity  $u_r$ ,  $u_\phi$  and  $u_z$  as functions of  $r$  and  $z$ .

### 2.1. Temporal discretization: operator splitting

A second-order time-accurate operator splitting procedure (Rigopoulos 1998) was applied to the equations which treated the contributions from the nonlinear (convection) terms, pressure terms and linear (viscous) terms, in three fractional steps.

The first fractional time step accounts for the nonlinear term and uses an explicit, second-order Adams–Bashforth approximation:

$$U^{l+1/3} = U^l - \Delta t \left( \frac{3}{2}(U^l \cdot \nabla)U^l - \frac{1}{2}(U^{l-1} \cdot \nabla)U^{l-1} \right). \quad (2.1)$$

Here,  $l$  denotes the time level and  $\Delta t$  the timestep.

The second fractional time step adjusts the velocity according to the pressure gradient:

$$\mathbf{U}^{l+2/3} = \mathbf{U}^{l+1/3} - \Delta t \nabla P^{l+1}. \quad (2.2)$$

However, in order to do this, the pressure  $P^{l+1}$  is solved using the Poisson equation

$$\nabla^2 P^{l+1} = \frac{1}{\Delta t} \nabla \cdot \mathbf{U}^{l+1/3} \quad (2.3)$$

which is obtained by applying the incompressibility constraint on  $\mathbf{U}^{l+2/3}$  and taking the divergence of (2.2). Neumann boundary conditions were used for the pressure at the inner and outer radii. First-order time-accurate Neumann boundary conditions lead to second-order time-accurate velocity (Karniadakis, Israeli & Orszag 1991). A first-order time-accurate Neumann boundary condition at the cylinder walls can be obtained by taking the inner product of the Navier–Stokes equations with the boundary normal vector to give

$$\frac{\partial P^{l+1}}{\partial r} = -\frac{1}{Re} (\nabla \times (\nabla \times \mathbf{U}^l))_r - (\mathbf{U}^l \cdot \nabla) u_r^l. \quad (2.4)$$

Periodic boundary conditions are used in the axial direction for the pressure.

The third fractional time step accounts for the viscous term contribution:

$$\mathbf{U}^{l+1} = \mathbf{U}^{l+2/3} + \frac{1}{Re} \Delta t \left( \left( \frac{1}{2} + \theta \right) \nabla^2 \mathbf{U}^{l+1} + \left( \frac{1}{2} - \theta \right) \nabla^2 \mathbf{U}^l \right). \quad (2.5)$$

where the implicit  $\theta$ -scheme is used. This scheme reverts to the first-order backward-Euler method for  $\theta = 0.5$  and the second-order Crank–Nicolson method for  $\theta = 0$ . A small but non-zero value of  $\theta$  is typically used to suppress high-frequency oscillations that are neutrally stable for the Crank–Nicolson scheme. The choice of  $\theta$  is discussed in §2.3 on temporal accuracy.

Each velocity component requires the solution of a Helmholtz equation with the Dirichlet boundary conditions:

$$\mathbf{U}^{l+1}(r_{in}, \phi, z, t) = (0, V(t), 0) \quad (2.6)$$

and

$$\mathbf{U}^{l+1}(r_{out}, \phi, z, t) = (0, 0, 0). \quad (2.7)$$

Periodic boundary conditions were used in the axial and azimuthal directions for the velocity components.

## 2.2. Spatial discretization: spectral method

To represent the velocity components and the pressure, a complex Fourier expansion was used in the axial direction with  $M$  Fourier planes spanning the axially periodic domain of aspect ratio  $\Gamma$ . A Chebyshev approximation was used in the radial direction with  $N$  points. A Fourier–Chebyshev derivative transform routine was used to evaluate the derivatives that were explicit in each fractional step.

A Poisson solver was developed which solved (2.3) for the pressure. A Helmholtz solver was developed which solved (2.5) for the radial and azimuthal components of velocity separately. Another modified Helmholtz solver was developed which solved (2.5) for the axial component of velocity. These solvers were based on a spectral-Tau method. In this approach, the equations were expressed in spectral space. However, the equations were first rewritten to have factors proportional to  $r$  and  $r^2$  in front of the derivatives because these factors have spectral coefficients which were easily

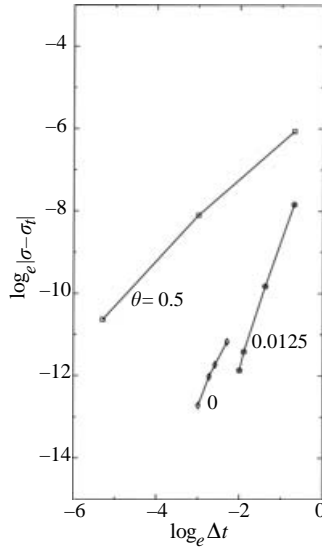


FIGURE 2. Time-accuracy of schemes with different  $\theta$ .

derived analytically. The solutions to the spectral coefficients were determined after  $M$  inversions of matrices of size  $(N - 2) \times (N - 2)$ . The  $M$  matrix inversions are only done once for each solver in a preprocessing step. The spectral solution is inverse transformed to obtain the real space solution. The algorithm is similar to the approach taken by Haidvogel & Zang (1979) who applied it to Cartesian geometries.

### 2.3. Accuracy

The case  $\eta = 0.5$ ,  $\mu = 0$ ,  $Re = 74.924 = 1.10Re_c$ ,  $\lambda = 1.988$  was considered. The grid size was  $16 \times 17$ . The time-accuracy was verified by using the referenced value (Marcus 1984) of growth rate  $\sigma_t = 0.035636$  for this case. Figure 2 shows the time-accuracy for various choices of the weighting parameter  $\theta$ . The choice of  $\theta = 0.5$  demonstrates the expected first-order time-accuracy because the slope is approximately one. Use of the Crank–Nicolson scheme for the viscous step, i.e.  $\theta = 0$ , results in second-order time-accuracy as the slope is approximately two. However, in this case, the use of a large  $\Delta t$  leads to numerical error in the form of temporal oscillations (Karniadakis *et al.* 1991). By choosing a suitably small value of  $\theta$ , this problem can be overcome. This is shown in figure 2 for  $\theta = 0.0125$  where the line extends into the region of large  $\Delta t$ . The calculated growth rate from a  $32 \times 33$  grid differed by less than 3 parts in  $10^{-5}$ , indicating that a  $16 \times 17$  grid resolves the flow spatially.

## 3. Results

We considered an inner cylinder Reynolds number which was linearly increased in time from an initial subcritical  $Re_i$  to a final supercritical value  $Re_f$  over a ramp time  $T$  (given in terms of inner cylinder rotations), and then kept constant at  $Re_f$ . The value of  $Re_f$  was generally taken to be not far above  $Re_c$ . A number of different simulations were conducted for fixed  $Re_i$ ,  $Re_f$  and different  $T$ . In each simulation, initial conditions of circular Couette flow plus a random perturbation of the relative order  $10^{-4}$  was applied. A random perturbation of this order was considered

since we felt this may be typical of the expected noise level of a physical experiment. The random number generation sequence was kept the same for each simulation to ensure that initial conditions were fixed.

We calculated the mode amplitudes  $A_\lambda(t)$  from the Fourier transform of the radial component of velocity at the radial centre of the gap,

$$A_\lambda(t) = \sqrt{\hat{u}_r^2(r_c, m, t)_{real} + \hat{u}_r^2(r_c, m, t)_{imag}}, \quad (3.1)$$

where the allowed discrete wavelengths are given by

$$\lambda = \Gamma/m \quad \text{for} \quad m = 1, \dots, M/2 - 1, \quad (3.2)$$

where  $m$  is the axial Fourier index.

The following choice of parameter values were made:  $\eta = 0.727$ ,  $\mu = 0$ ,  $Re_i = 70$  and  $Re_f = 116.67$ . Note that this value of  $\eta$  was chosen because Burkhalter & Koschmieder (1973, 1974) demonstrated experimentally that stable Taylor-vortex flow existed for  $Re/Re_c$  up to 9 for both quasi-steady increases and sudden starts. In addition, the stability analysis of Jones (1984), and Antonijoan & Sanchez (2002) showed the axisymmetric Taylor-vortex flow exists for  $Re/Re_c < 4.5$  at the critical wavelength. Thus, this choice of  $\eta$  leads to axisymmetric Taylor-vortex flow as the final state for the choice of  $Re_f$ . Koschmieder (1993) presented results of minimum critical Reynolds number and critical wavelength versus radius ratio. Using linear interpolation, we calculated  $\lambda_c = 2.003$  and  $Re_{c,\lambda_c} = 82.79$  for radius ratio  $\eta = 0.727$ . The aspect ratio  $\Gamma = 20.03$  was set to be ten times larger than  $\lambda_c$ . This choice is large enough to guarantee different possible final states depending on the ramp time without making the cost of each simulation too expensive. While a longer aspect ratio would allow a finer gradation of allowable wavelengths, it would not change the interpretation of the results in terms of the linear model. The numerical parameters were set to  $M = 324$ ,  $N = 33$  and  $\Delta t = 0.1$ . However, for the smaller ramp times  $\Delta t$  had to be reduced by up to an order of magnitude for a short initial period of time in the simulation. This was done to adequately resolve the initial stage of fast decay due to viscous damping (Liu & Chen 1973).

Using (3.2), in the vicinity of  $\lambda_c$  we have the following allowed discrete wavelengths: 1.541, 1.669, 1.821, 2.003 and 2.225. Alternatively, these may be referred to as modes with  $m = 13, 12, 11, 10$  and  $9$ , respectively (corresponding to the number of Taylor vortices within the axial domain. In figure 3, we plot  $A_\lambda(t)$  for different ramp times  $T$  for these five modes. The inset graphs for  $T = 0$  and  $T = 5$  show a close-up of the region where the modes interact.

Figure 4 is a close-up of  $A_\lambda(t)$  for sudden starts, showing an initial stage of decay before exponential growth occurs.

Figure 5 is a plot of instantaneous growth rate versus instantaneous Reynolds number during the Reynolds number ramp. The inset graphs show a close-up of the intersections on the Reynolds number axis.

Figure 3 shows that  $\lambda_c$  is preferred for sufficiently long ramp times, as illustrated for  $T = 100$  and  $T = 150$ . For sudden starts,  $T = 0$ , the preferred wavelength  $\lambda = 1.669$  is less than  $\lambda_c$ . The selected wavelength changes from 1.669 to 1.821 to 2.003 for progressively longer ramp times. The wavelengths of these three Taylor-vortex flow states lie within the Eckhaus stable band. This trend agrees with the observed behaviour from physical experiments reported by Koschmieder (1993).

It is evident from figure 4 that, for sudden starts, the amplitude of each mode did not begin to grow exponentially. There was a short initial period of time of decay

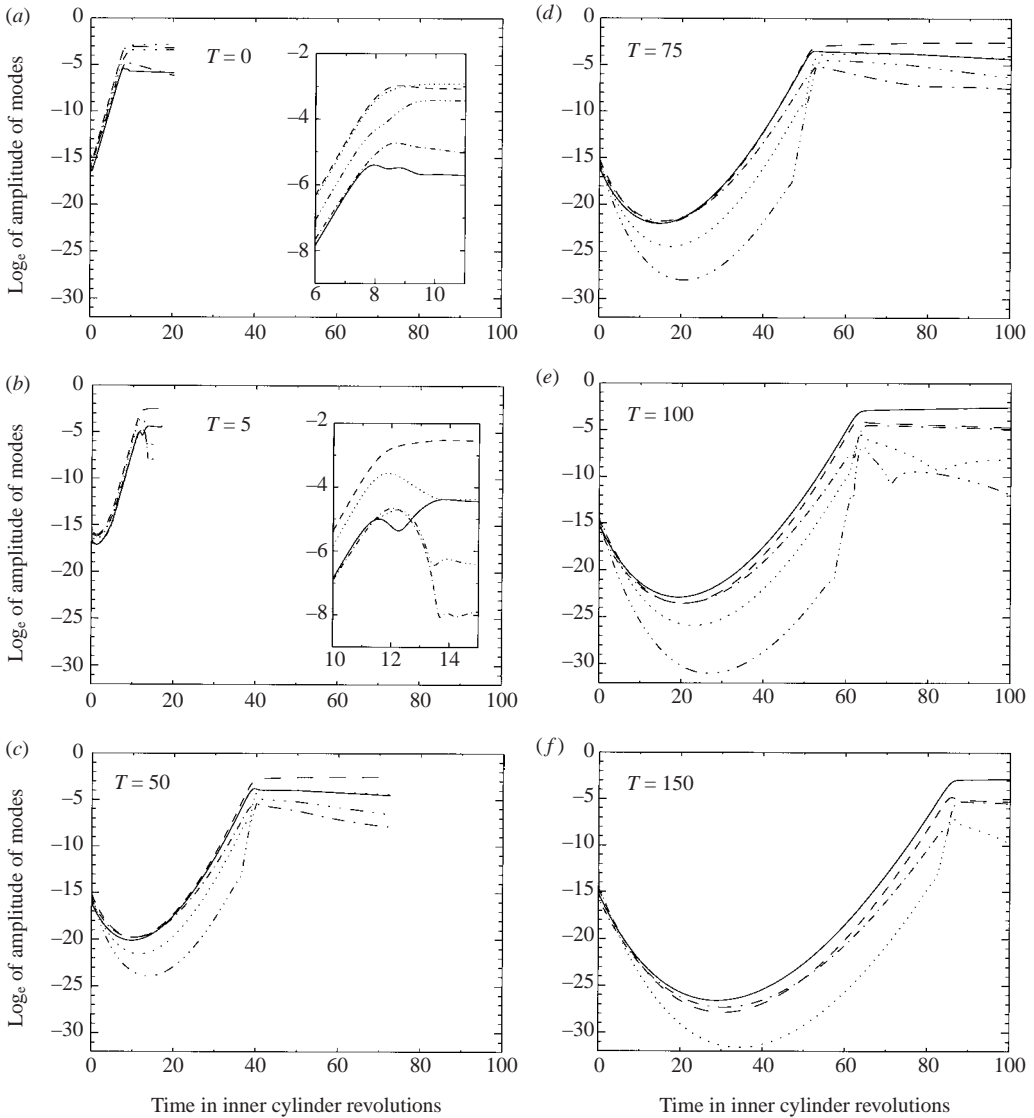


FIGURE 3.  $A_\lambda(t)$  for six different ramp times  $T$ .  $\dashdot$ ,  $\lambda_c = 2.225$ ;  $\text{—}$ ,  $\lambda_c = 2.003$ ;  $\text{---}$ ,  $\lambda_c = 1.821$ ;  $\cdots$ ,  $\lambda_c = 1.669$ ;  $\text{-}\cdot\text{-}\cdot\text{-}$ ,  $\lambda_c = 1.541$ .

before exponential growth began. This initial decay has been attributed to viscous damping (Liu & Chen 1973). During this time, the base flow has been perturbed from circular Couette flow and is unsteady. Once the base flow readjusts, the amplitude of the modes begin to grow exponentially.

#### 4. Linear model

If the initial perturbation is expressed as a weighted sum of eigenfunctions of the linearized form of the equations, then the weighting factors assign a value for the initial amplitude of magnitude  $A_\lambda(0)$  for each mode. For our numerical studies, we

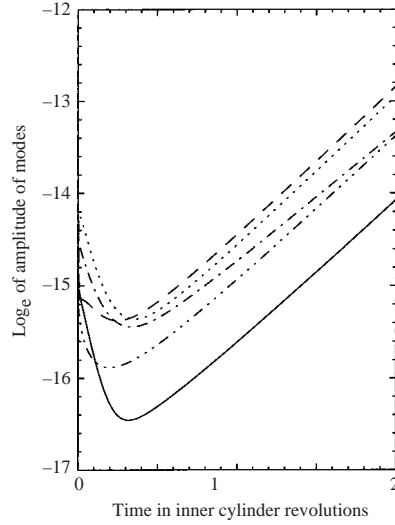


FIGURE 4.  $A_\lambda(t)$  for sudden starts.  $\cdots$ ,  $\lambda = 2.225$ ;  $\text{—}$ ,  $\lambda_c = 2.003$ ;  $-\text{--}$ ,  $\lambda = 1.821$ ;  $\cdots$ ,  $\lambda = 1.669$ ;  $-\cdots$ ,  $\lambda = 1.541$ .

consider the initial mode amplitudes  $A_\lambda(0)$  to apply at the time after the base flow has readjusted and the modes begin their independent stage of growth.

#### 4.1. Constant $Re$

If the  $A_\lambda(0)$  are small, each mode will either grow or decay exponentially, depending on whether the wavelength is inside or outside the band from linear stability theory.

As the modes grow independently of each other, for a constant Reynolds number, we can write

$$A_\lambda(t) = A_\lambda(0) \exp(\sigma_\lambda t). \quad (4.1)$$

Equation (4.1) is the solution to the Landau equation in its simplest form

$$\frac{dA_\lambda}{dt} = \sigma_\lambda A_\lambda. \quad (4.2)$$

In figure 5, when  $T$  is increased (or the rate of increase of  $Re$  is decreased)  $\sigma_\lambda$  approaches a linear relationship with  $Re$ . The growth rate can be written as linearly proportional to Reynolds number (Drazin & Reid 1989), provided it is not too far from the critical Reynolds number. Assigning the critical Reynolds number and cofactor of proportionality with mode-dependency, we have

$$\sigma_\lambda = K_\lambda (Re - Re_{c,\lambda}). \quad (4.3)$$

In figure 5, the lines of  $\sigma_\lambda$  versus  $Re$  intersect each other. Therefore the value of the slope,  $K_\lambda$ , is different for each mode. Which mode has the greatest instantaneous growth rate depends on the value of  $Re$ . Indeed, the ordering of the growth rates of each mode, greatest to smallest, varies with  $Re$ . Analysis of figure 5 shows that in the linear part of the plot,  $K_\lambda$  increases with decreasing  $\lambda$ .

The values of  $K_\lambda$  and  $Re_{c,\lambda}$  could be determined from a linear stability analysis. Alternatively, results from a sufficiently long ramp time can be used. Table 1 shows these values for the  $T = 100$  case. Subsequently, (4.3) can be used to predict the values of  $\sigma_\lambda$  for each mode as a function of  $Re$ .



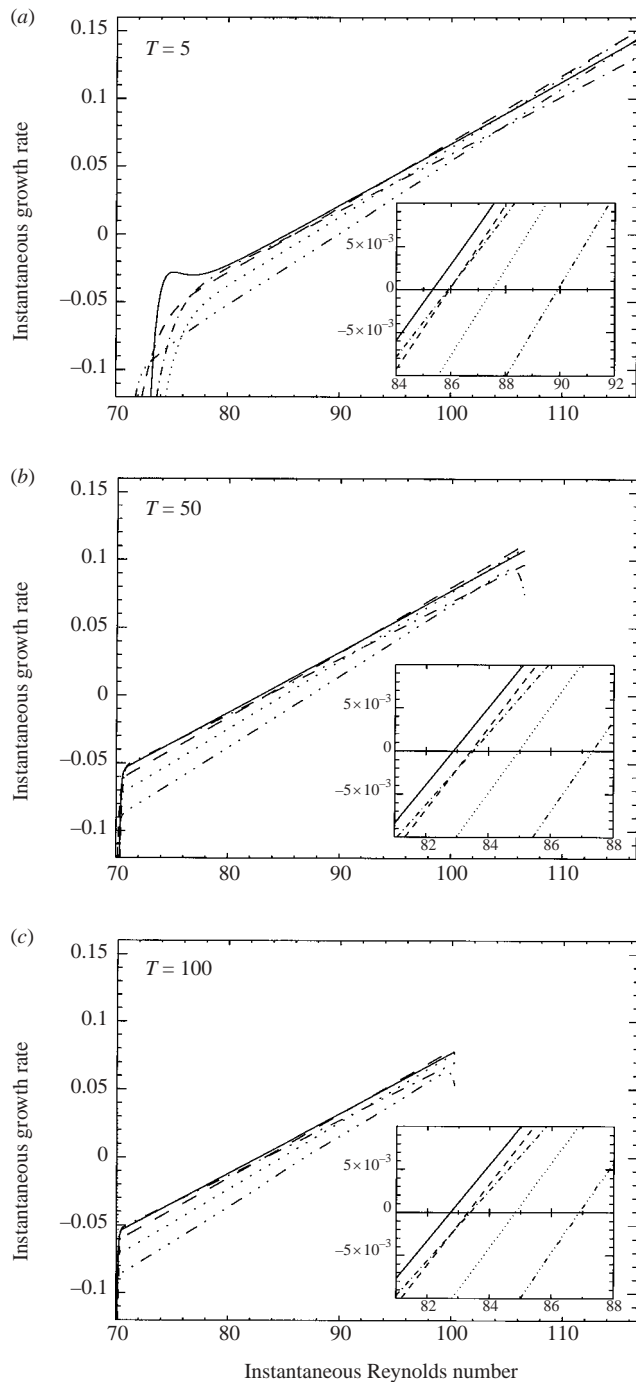


FIGURE 5. Instantaneous  $\sigma_i(t)$  versus instantaneous  $Re(t)$  for three different ramp times.  $\cdots$ ,  $\lambda = 2.225$ ;  $\text{—}$ ,  $\lambda_c = 2.003$ ;  $\text{---}$ ,  $\lambda = 1.821$ ;  $\text{-}\cdot\text{-}$ ,  $\lambda = 1.669$ ;  $\text{---}$ ,  $\lambda = 1.541$ .

#### 4.2. Linearly increasing $Re(t)$

It will be assumed that the instantaneous growth rate  $\sigma_i(t)$  at a particular  $Re$  during a ramp is equal to the growth rate when  $Re$  is held fixed at that particular value. The

---

Mode number ( $m$ )	$Re_{c,\lambda}$	$K_\lambda$
9	83.4	0.0041
10	82.8	0.0044
11	83.3	0.0047
12	84.8	0.0050
13	86.9	0.0052

---

TABLE 1. Critical Reynolds numbers ( $Re_{c,\lambda}$ ) and growth rate slope ( $K_\lambda$ ) for the  $T = 100$  ramp case (refer to figure 5c).

---

results of Eagles (1971) and Neitzel (1982), who have studied the stability of unsteady circular Couette flow, have indicated that this assumption would gradually break down as the acceleration rate is increased to large values. Indeed, this behaviour is clear from the insets of figure 5. In fact, comparison of figure 5(a) with 5(c) shows that the instantaneous critical Reynolds numbers for each mode increase with larger acceleration rates. When  $T = 100$ , the critical Reynolds number for  $\lambda_c$  is 82.8, agreeing with the result 82.79 from Koschmieder (1993), obtained by keeping the value of  $Re$  fixed. For  $T = 5$ , the instantaneous critical Reynolds number for each mode is uniformly increased by about 3%.

Proceeding with our assumption then, we must solve

$$\frac{dA_\lambda}{dt} = \sigma_\lambda(t)A_\lambda, \quad (4.4)$$

which becomes

$$A_\lambda(t) = A_\lambda(0) \exp\left(\int_0^t \sigma_\lambda(t') dt'\right), \quad (4.5)$$

where from (4.3)

$$\sigma_\lambda(t) = K_\lambda(Re(t) - Re_{c,\lambda}). \quad (4.6)$$

The linear ramp is defined to start from  $t = 0$ . The ramp function  $Re(t)$  can be defined as

$$Re(t) = \begin{cases} Re_i + \frac{dRe}{dt}t & \text{if } t \leq T, \\ Re_f & \text{if } t > T, \end{cases} \quad (4.7)$$

where the ramp rate is

$$\frac{dRe}{dt} = \frac{Re_f - Re_i}{T}. \quad (4.8)$$

In terms of the instantaneous exponential growth rate we have

$$\sigma_\lambda(t) = \begin{cases} -\sigma_{o,\lambda} + C_\lambda t & \text{if } t \leq T, \\ \sigma_{f,\lambda} & \text{if } t > T, \end{cases} \quad (4.9)$$

where

$$\sigma_{o,\lambda} = -K_\lambda(Re_i - Re_{c,\lambda}) \quad (4.10)$$

and

$$\sigma_{f,\lambda} = K_\lambda(Re_f - Re_{c,\lambda}). \quad (4.11)$$

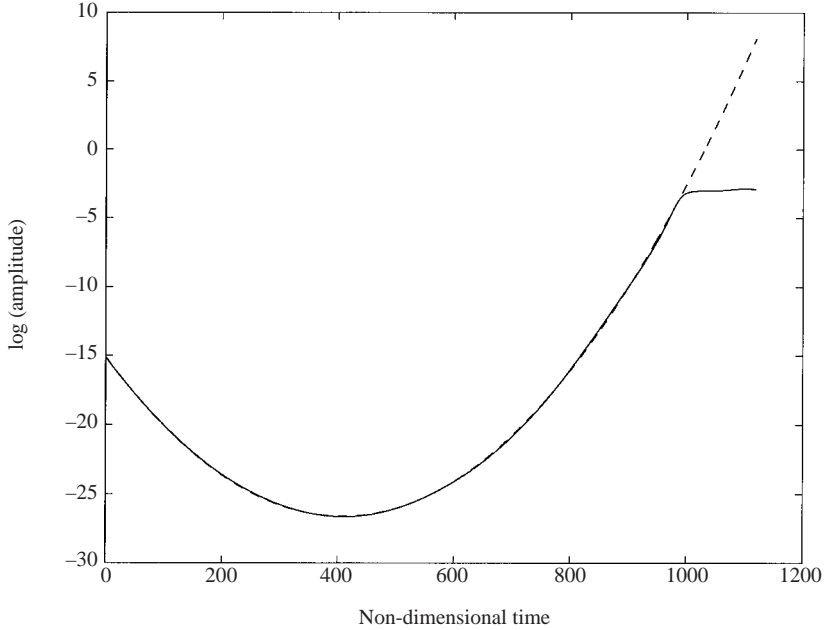


FIGURE 6. Comparison of the time variation of the amplitude of the  $\lambda_c = 2.003$  mode from the numerical calculations and the linear theory (equation (4.13)). Here,  $T = 150$ . The fit is effectively exact almost until saturation.

A consequence of using an  $Re$  ramp rate is that each mode has a particular rate of change of growth rate  $C_\lambda$ , where

$$C_\lambda = K_\lambda \frac{dRe}{dt}. \quad (4.12)$$

The solution of (4.4) after substitution of (4.9) for  $\sigma_\lambda(t)$  gives

$$A_\lambda(t) = \begin{cases} A_\lambda(0) \exp(-\sigma_{o,\lambda}t + \frac{1}{2}C_\lambda t^2) & \text{for } t \leq T, \\ A_\lambda(0) \exp(\frac{1}{2}(\sigma_{f,\lambda} - \sigma_{o,\lambda})T + \sigma_{f,\lambda}(t - T)) & \text{for } t > T. \end{cases} \quad (4.13)$$

The logarithm of the amplitude of the modes will therefore vary quadratically in time during the ramping stage. During the linear ramp in Reynolds number, the instantaneous growth rate for a mode increases linearly from an initial negative value through zero to a final positive value. Therefore, during the ramp, the logarithm of the amplitude of the mode decays quadratically to some minimum amplitude then grows quadratically to a higher amplitude. These features agree with the behaviour of the modes in their independent stage of growth shown in figure 3. A stronger comparison is provided by figure 6. This shows the predicted fit from the linear theory (equation (4.13)) and the numerical prediction, for the dominant mode ( $\lambda = 2.003$ ) for a ramp time of  $T = 150$  (also shown in figure 3f). The fit is visually perfect almost until saturation, verifying the applicability and validity of the linear theory.

Now, consider the total time,  $t_\lambda^*$  that it takes for the amplitude of each mode  $\lambda$  to grow to a particular higher amplitude  $A^*$ . In particular, this could represent the amplitude necessary for the mode(s) to begin to interact nonlinearly. From (4.13), we

obtain

$$t_{\lambda}^* = \begin{cases} \frac{1}{\sigma_{f,\lambda}} \ln\left(\frac{A^*}{A_{\lambda}(0)}\right) + \frac{T}{2} \left(1 + \frac{\sigma_{o,\lambda}}{\sigma_{f,\lambda}}\right) & \text{if } t_{\lambda}^* \geq T, \\ \frac{1}{C_{\lambda}} \left(\sigma_{o,\lambda} + \sqrt{\sigma_{o,\lambda}^2 + 2C_{\lambda} \ln(A^*/A_{\lambda}(0))}\right) & \text{if } t_{\lambda}^* < T. \end{cases} \quad (4.14)$$

For simplicity of the argument, let us assume the initial amplitudes of the modes are the same so that no particular mode is favoured initially. This would be the case if the initial perturbation were constructed as an equally weighted sum of the linear eigenfunctions of each mode.

Consider the first expression on the right-hand side of (4.14). The first term represents the time it takes for each mode to reach  $A^*$  for impulsive starts,  $t_{\lambda}^*, \text{impulsive}$ . The second term represents an additional time delay,  $t_{\lambda}^*, \text{ramp}$ , for each mode due to the ramp.

Now  $t_{\lambda}^*, \text{impulsive}$  has a shortest-to-longest ordering for each mode according to the highest-to-lowest ordering of the final exponential growth rates  $\sigma_{f,\lambda}$  for each mode. This follows from the factor  $1/\sigma_{f,\lambda}$  in the first term. The values of  $\sigma_{f,\lambda}$  as a function of  $Re_f$  are given by (4.11).

Also,  $t_{\lambda}^*, \text{ramp}$  has a shortest-to-longest ordering corresponding to the lowest-to-highest ordering of the critical Reynolds number  $Re_{c,\lambda}$  for each mode. This follows from the factor

$$1 + \frac{\sigma_{o,\lambda}}{\sigma_{f,\lambda}} = 1 + \frac{Re_{c,\lambda} - Re_i}{Re_f - Re_{c,\lambda}} = \frac{Re_f - Re_i}{Re_f - Re_{c,\lambda}} \quad (4.15)$$

in the second term, which has a smallest-to-largest ordering corresponding to the lowest-to-highest ordering of the critical Reynolds number  $Re_{c,\lambda}$  for each mode. The values  $Re_{c,\lambda}$  are given by the neutral stability curve from linear stability analysis, as illustrated by the outer curve in figure 1. For the slow ramp case ( $T = 100$ ) shown in figure 5(c) the critical Reynolds numbers and growth rate slopes are given in table 1. The highest-to-lowest ordering of  $\sigma_{f,\lambda}$  is not the same as the lowest-to-highest ordering of  $Re_{c,\lambda}$ .

When the ramp time is increased from the impulsive start situation ( $T = 0$ ) to the situation with very slow increases ( $T$  very large),  $t_{\lambda}^*, \text{ramp}$  becomes progressively more significant in relation to  $t_{\lambda}^*, \text{impulsive}$ . The shortest-to-longest ordering of  $t_{\lambda}^*$  gradually changes from the highest-to-lowest ordering of  $\sigma_{f,\lambda}$  to the lowest-to-highest ordering of  $Re_{c,\lambda}$ .

For sufficiently large ramp times the shortest-to-longest ordering of  $t_{\lambda}^*$  will always be according to the lowest-to-highest ordering of  $Re_{c,\lambda}$ . The smallest value being  $t_{\lambda_c}^*$ . These features are observed in figure 3 for  $T = 100$  and  $T = 150$  in the portion of the independent stage of growth before nonlinear effects occur.

As the ramp time is increased further, the mode with the critical wavelength will grow to  $A^*$  progressively earlier than the other modes. In this sense, the critical wavelength is being increasingly favoured, above all other modes.

In fact, the second expression on the right-hand side of (4.14) applies for very long ramp times. For  $T$  large, the expression can be approximated by

$$t_{\lambda}^* = \frac{2T(Re_{c,\lambda} - Re_i)}{Re_f - Re_i} \left(1 + O\left(\frac{1}{T}\right)\right) \quad \text{if } t_{\lambda}^* < T, T \gg 1. \quad (4.16)$$

Hence, in agreement with the former analysis, the shortest-to-longest ordering of  $t_{\lambda}^*$  will always be according to the lowest-to-highest ordering of  $Re_{c,\lambda}$ .

Mode number ( $m$ )	$t_\lambda^*$			
	$T=0$	$T=50$	$T=100$	$T=150$
9	9.35	41.69	67.67	92.50
10	8.19	38.85	63.26 <sup>†</sup>	86.70 <sup>†</sup>
11	7.65	38.80 <sup>†</sup>	64.07	88.47
12	7.15 <sup>†</sup>	40.62	68.94	96.59
13	7.18	44.65	77.81	110.43

TABLE 2. Linear amplification times ( $t_\lambda^*$ ) for different ramp times (expressed in units of cylinder rotations). The linear analysis predicts that the mode selection will correspond with minimum growth times. <sup>†</sup> Mode selection from the numerical experiments.

Table 2 shows the predicted values of  $t_\lambda^*$  using the parameters from table 1 for different ramp times. According to the linear theory, for each mode, the minimum growth time should correspond with the selected mode. The actual selected modes for the numerical experiments are shown by the dagger symbol. For these calculations, the initial amplitudes are measured for each of the modes from the numerical experiments by extrapolating the amplitudes back to the initial time. The initial amplitudes are approximately  $\exp(-15)$  within  $\pm 0.5$  in the logarithm. For each of the ramp times shown, the mode selected in the numerical experiments corresponds to the mode predicted by the linear theory. Note that there is reasonable sensitivity to the initial amplitude for ramp times shorter than about 50 cylinder revolutions.

## 5. Nonlinear effects

Suppose the discrepancy due to variations in the  $\sigma_\lambda(t)$  versus  $Re(t)$  linear profile for high ramp rate is disregarded (compare figures 5a and 5c). We can redefine  $t_\lambda^*$  as the time it would take a pure mode perturbation with wavelength  $\lambda$  to grow to an amplitude  $A_\lambda^*$  where nonlinear self-interaction begins. Then  $t_{\lambda,ramp}^*$  represents the delay time for mode  $\lambda$  to grow to  $A_\lambda^*$ . The change in the ordering of  $t_\lambda^*$  with ramp time influences which state will be preferred at steady state.

From figure 3,  $\lambda=1.669$  is the preferred mode when  $T=0$ . For  $T=5$ , the delay time for  $\lambda=1.669$  is sufficiently greater than the delay time for  $\lambda=1.821$  so the  $\lambda=1.821$  mode has time to self-interact and approach the form of a steady-state Taylor-vortex flow. Consequently the  $\lambda=1.66905$  mode and the remaining modes react as if they are small perturbations to that Taylor-vortex flow, and decay. Thereby a stable Taylor-vortex flow with  $\lambda=1.821$  is achieved.

Similarly for  $T=100$ , the difference in delay time between the  $\lambda=1.821$  mode and the  $\lambda=2.003$  mode is great enough so that the  $\lambda=2.003$  mode has time to self-interact and approach the form of a steady-state Taylor-vortex flow. Consequently, the  $\lambda=1.821$  mode and the remaining modes react as if they are small perturbations to that Taylor-vortex flow, and decay. Thereby a stable Taylor-vortex flow with  $\lambda=2.003$  is achieved.

As the ramp time is increased past  $T=100$ , the delay time for the  $\lambda=2.003$  mode will decrease relative to the delay time for the other modes. Thus, the  $\lambda=2.003$  mode will increasingly have more time to self-interact and approach the form of a steady-state Taylor-vortex flow. This is a partial explanation as to why the mode with

the critical wavelength is always preferred when the inner cylinder Reynolds number is increased quasi-steadily from subcritical to supercritical values.

This can be summarized as follows. When the ramp time is very short, the mode with the maximum growth rate at the final Reynolds number is selected. For long ramp times, the second term in (4.14) must dominate, which is smallest for the critical wavelength. Effectively, the mode with the critical wavelength has time to grow to high amplitudes before the other modes begin to be amplified. This is true even if the growth rate curves cross over at subcritical Reynolds numbers, so that the critical mode is initially damped faster than some other mode. Also note that this is independent of the initial amplitude of each mode. On the other hand, the conclusion for impulsive starts does rely on equal initial amplitudes of the modes (which is likely to be approximately true).

## 6. Effect of finite aspect ratio

The numerical model as used in this paper restricts the aspect ratio and assumes periodicity in the axial direction. The effect of these two choices is considered in this section.

The restriction to a finite aspect ratio means this problem is different to the idealized case of an infinite aspect ratio. Finite aspect ratio causes the Fourier spectrum of allowed axial wavelengths to be discrete, unlike in the infinite case where it is continuous. However, experimental rigs, of course, have finite aspect ratios and effectively this means that the allowed spectrum is discrete, as the number of Taylor vortices must be an integer in the final equilibrium state, even though the size of the Taylor-vortex cells may not be constant. On the other hand, the boundaries at the ends of experimental Taylor–Couette rigs enforce different boundary conditions from the idealized case examined in this article; generally either fixed, corotating or free ends. The influence of boundary conditions can be significant. In particular, the critical Reynolds number is affected and the mode transition boundaries can be shifted considerably. An example of the effects can be seen in the experimental results of Xiao *et al.* (2002). They used constant acceleration to move from a subcritical to a supercritical state, as is done here, and found the final state was a strong function of the aspect ratio. However, unlike the case presented here, they used a smaller gap size where the transition to wavy Taylor-vortex flow occurs for Reynolds numbers only slightly above that for Taylor-vortex transition. Aspect ratios up to 50.54 were used. They did find the character of the final state, i.e. either wavy Taylor-vortex flow or Taylor-vortex flow with a smaller than critical wavelength, appeared to become less sensitive to aspect ratio as the aspect ratio was increased.

To investigate the effect of non-periodic boundary conditions, further simulations have been performed replacing the periodicity condition with non-slip boundary conditions at the ends of the axial domain. This is not possible with the spectral code used for the bulk of the results in this paper, so two other independent codes were used for this study. These were a Galerkin third-order (spatially accurate) finite-element code used to obtain steady-state results, and a second-order (time-accurate) spectral-element code for time-dependent simulations. Both codes have been carefully validated for related problems (e.g. Hourigan, Graham & Thompson 1998; Thompson, Hourigan & Sheridan 1996). In addition, both codes can enforce periodic boundary conditions in the axial direction and so a direct validation against the results from the fully spectral code was possible. For each code, the grid sizes

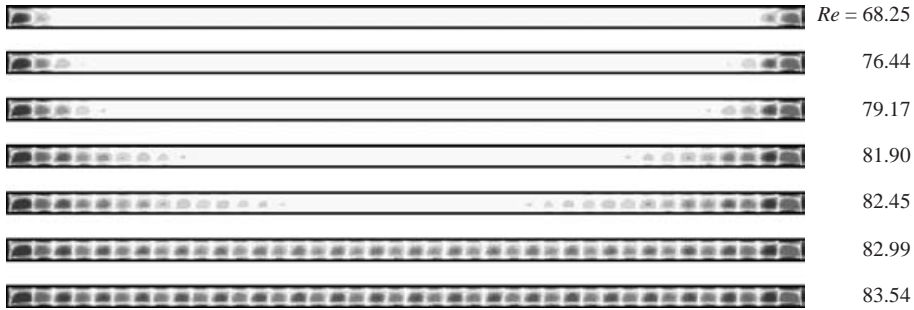


FIGURE 7. Greyscale plots of vorticity showing the effect on non-slip boundary conditions on equilibrium solutions for a finite aspect ratio. The critical Reynolds number in this case is 82.79. As this critical Reynolds number is approached, the vortices induced by the end conditions affect more of the domain. The vorticity levels are the same for each plot.

were adjusted so that the critical Reynolds number was predicted to within better than 0.1%.

Figure 7 shows the effect of non-slip ends obtained using the steady code as a function of Reynolds number. The aspect ratio was  $\Gamma = 40.06 = 20\lambda_c$ . The critical Reynolds number for periodic end conditions is 82.79. The greyscale contours show the development of vortices at the ends of the axial domain at Reynolds numbers significantly less than critical. However, the transition in the middle section of the domain occurs at close to the ideal critical Reynolds number.

Hence, at least for the equilibrium solutions, the effect of the non-slip boundaries does not appear to influence the critical Reynolds number at the centre of the domain very significantly. (Admittedly, the numerical results show that very weak Taylor vortices occur even near the centre of the domain at Reynolds numbers considerably below critical; these are not seen on the plots in figure 7 because of the levels chosen, however, it is only close to  $Re_c$  that the magnitudes of the vorticity become significant.) These conclusions are consistent with the earlier numerical simulations of De Roquefort & Grillard (1978).

To further quantify the effect of the alternative boundary conditions, time-dependent simulations at post-critical Reynolds numbers were performed to determine the timescale for propagation of boundary effects towards the centre of the domain relative to the timescale for growth of Taylor vortices when periodic boundary conditions are used. Figure 8 shows the time-dependent development of the Taylor-vortex flow starting from rest for an aspect ratio of  $\Gamma = 80.12 = 40\lambda_c$ , and  $Re = 116.67$  (the final Reynolds number for the spectral simulations). The effect of the end vortices is to cause the neighbouring vortices to spin up prematurely. This effect propagates from the ends of the domain towards the centre. In parallel with this, the Taylor-vortex cells in the middle region of the domain are growing independently, so that at non-dimensional time 175 ( $= 10.45$  inner cylinder rotations) the middle half of the domain shows simultaneous development of Taylor vortices of similar strength. There is no applied perturbation in this simulation; the development of the vortices is seeded by computer roundoff error. The number of vortex pairs is 45, considerably higher than that predicted for quasi-steady increases of 40. Thus, it appears that for sudden starts and small ramp times, the growth of Taylor vortices away from the boundaries will be relatively unaffected by end boundary conditions. For those vortices near the ends, whose growth rate is enhanced, it seems likely that the selected wavelength is predominately determined by the Reynolds number rather than end

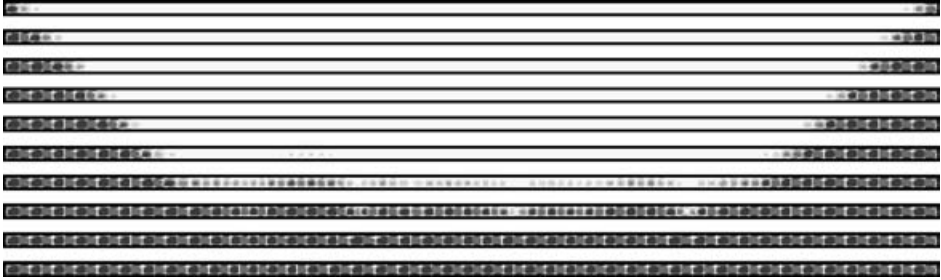


FIGURE 8. Development of Taylor-vortex flow after an instantaneous increase in Reynolds number from 70 to 116.67 as depicted by greyscale azimuthal vorticity. From top to bottom, the cross-sections correspond to non-dimensional times:  $t=0, 25, 50, 75, 100, 125, 150, 175, 250$  and  $500$ . Fixed end conditions are used. The aspect ratio was  $\Gamma = 80.12$  corresponding to 40 critical wavelengths.

effects. Supporting evidence comes from a comparison of simulations using the two types of end condition. For the case with periodic boundaries, the selected number of vortex pairs is also 45, as it is for the non-slip boundary case. Hence, it appears wavelength selection for Taylor-vortex flow, at least for reasonable aspect ratios, is insensitive to end conditions.

Simulations at  $Re = 84.6$  (about 2% above critical) also support this view. For both types of boundary condition the final number of Taylor-vortex cells was 40 which is the most amplified mode from linear theory (Koschmieder 1993).

#### 6.1. Taylor-vortex development with constant acceleration rates and different end conditions

Simulations corresponding to different ramp times were made using the spectral-element method for both periodic and fixed end conditions to determine better the effect of the end conditions on the evolution. As for the fully spectral simulations, the inner cylinder rotation rate was linearly increased during the ramp time so that the Reynolds number varied between  $Re_i = 70$  and  $Re_f = 116.67$ . Once the final Reynolds number was reached the inner cylinder rotation rate remained fixed until the flow reached an equilibrium state. Once again, the initial flow corresponded to stationary Couette flow plus a random perturbation of relative magnitude  $10^{-4}$ . The same random number sequence was used for both cases, hence the velocity perturbation was identical even though the base flows were not. The aspect ratio for these simulations was  $\Gamma = 80.12$ , so that the axial domain was  $40\lambda_c$ .

The number of Taylor-vortex pairs contained in the domain for different ramp times is shown in figure 9. Interestingly, the same number of vortex pairs is observed for the two different boundary types for both sudden starts and long ramp times corresponding to quasi-steady increases. This is consistent with the results above. For sudden increases, the most amplified wavelength is determined by the final Reynolds number and the effect of the fixed ends is minimal. For the fixed ends case, there are two strong vortices at the ends of the domain initially at  $Re = 70$ , but once the Reynolds number is instantaneously increased to 116.67 further development of Taylor vortices, whether assisted by the influence of the ends or through amplification of the random perturbation in the middle section of the domain, is determined by the amplification rates at the final Reynolds number. At the other extreme, quasi-steady increases select a wavelength close to critical. In this case, the flow evolution corresponding to the different boundary types is different. For fixed ends, Taylor



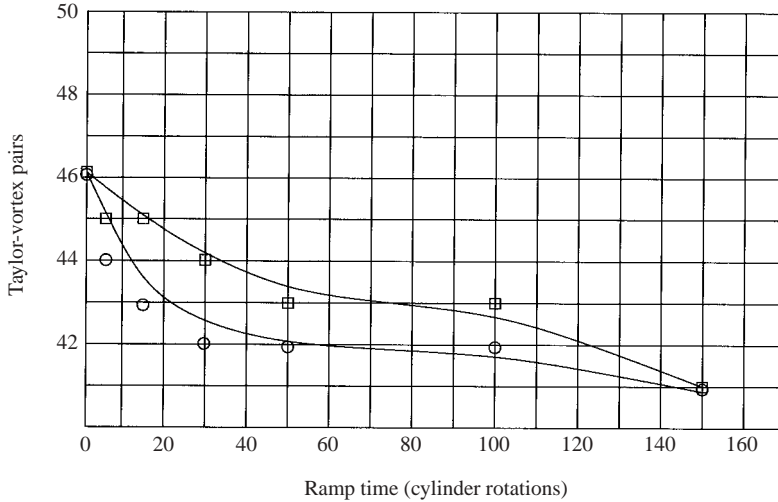


FIGURE 9. Number of Taylor-vortex pairs for different ramp times, for both periodic (squares) and fixed ends (circles). The aspect ratio was  $\Gamma = 80.1144$ , corresponding to 40 critical wavelengths. The dotted lines are only a visual guide to the dependence.

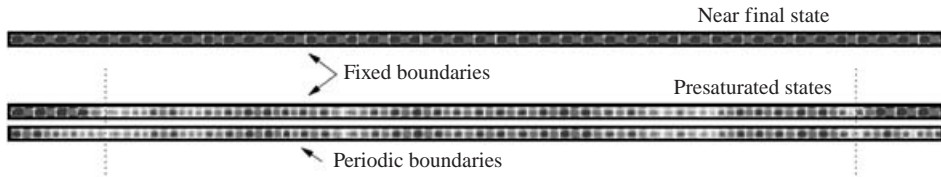


FIGURE 10. Taylor-vortex flow prior to saturation for both periodic and fixed end conditions for  $T = 5$ . Greyscale contours of azimuthal vorticity are used to indicate the flow state. The two lower plots show the effect of the end conditions on the developing Taylor-vortex flow. Between the dotted lines the flow state is near identical. The top vorticity plot shows the flow state after a long time ( $t = 2500$ ) after the local wavelength has attained a near uniform value throughout the axial domain.

vortices form more quickly at the boundaries. There is a reduced axial domain over which amplification of the initial velocity perturbation is the mechanism resulting in saturated Taylor vortices. For periodic end conditions only the second mechanism is active, hence all Taylor vortices saturate at close to the same time.

The results for the intermediate ramp times are more interesting. Between  $T = 5$  and 100, the selected mode is strongly dependent on end conditions. Fixed end conditions lead to fewer Taylor vortices (i.e. a longer wavelength). The qualitative reason for this is easy to understand. For intermediate ramp times, the Taylor vortices near the ends can grow and saturate well before the vortices in the central part of the domain. So the development and saturation of the vortices near the ends occurs at a lower average relative Reynolds number for which the fastest growing mode has a longer wavelength. Thus, fewer Taylor vortices are expected in the saturated state than for the equivalent case with periodic end conditions.

This leads to the obvious question: is the linear theory developed in this paper relevant to experimental results with other types of boundary conditions? To address this question consider figure 10. This shows snapshots of the vorticity field for  $T = 5$

for the two different types of end condition just prior to saturation at  $t = 70$ . (The end of the ramp occurs at  $t = 50$  in these units.) Recall that the initial velocity perturbation is the same in each case (even though the base flows are different). This figure shows that over most of the domain bounded by the dotted lines, the flow state is essentially identical. Thus, the flow over the majority of the domain has evolved independent of the end conditions until the vortices are close to their saturated strengths. Near the ends this is not the case. The flow for fixed ends has longer wavelength Taylor vortices because they developed when the average Reynolds number was lower and hence a longer wavelength was selected. Thus, it is expected that the linear theory should apply equally (albeit only over part of the domain) for both fixed and free ends.

For the fixed ends conditions, the flow between the dotted lines (figure 10) reaches (effective) saturation shortly afterwards. At this stage there is a mismatch in wavelength between the longer local wavelength at the ends and the shorter wavelength over the middle section of the domain. To account for this, there is a long time scale readjustment where the Taylor-vortex size becomes more uniform throughout the domain.

## 7. Nonlinear model

To account for nonlinear effects we suggest the addition of the following nonlinear terms to (4.4):

$$\frac{dA_i}{dt} = \sigma_i(t)A_i - l_i A_i |A_i|^2 - \sum_{j=1, j \neq i}^N \alpha_{ij} A_i |A_j|^2 + \sum_{j,q} \beta_{jq} A_j^* A_q^*, \quad (7.1)$$

for  $N$  modes where the asterisk denotes complex conjugate. The subscripts now denote Fourier indices. This model has been suggested by Abarbanel, Rabinovich & Sushchik (1993) for application to Rayleigh–Bénard convection.

In (7.1), the first cubic term accounts for the self-interaction of mode  $i$ . The second cubic term accounts for the coupling of mode  $i$  with other modes  $j$ . The effects of the cubic terms were described in §5. Effectively, they cause the modes to saturate by limiting the growth rate when the amplitudes become large. On the other hand, figure 3 shows rapid growth of some modes prior to saturation. It is speculated that the last term accounts for this behaviour.

The quadratic-term models resonant three-wave interactions. The index  $q$  is taken over all harmonics and is such that the resonance condition  $i + j = q$  is satisfied. Figure 3 shows that three-wave resonance effects appear as rapid regions of acceleration for lower amplitude modes prior to the saturation of the preferred mode.

Consider the Eckhaus mechanism of instability of a Taylor-vortex flow with a fundamental mode  $k$  and first harmonic  $q = 2k$ . When there are side-band perturbations with modes  $i$  and  $j$  such that  $i + j = 2k$ , these perturbations resonate with the first harmonic and mutually reinforce each other, destabilizing the Taylor-vortex flow. However, when we consider a Taylor-vortex flow within the Eckhaus stable band, the resonances still occur, but they are not strong enough to destabilize the flow.

We can illustrate the effect of the quadratic terms with a simple model with no Reynolds number ramp. Consider amplitude equations for four modes, the initial conditions being such that  $A_F(0) \gg A_H(0) \gg A_1(0) \gg A_2(0)$ :

$$\frac{d|A_F|}{dt} = \sigma_F |A_F|, \quad (7.2)$$

$$\frac{d|A_H|}{dt} = \sigma_H |A_H|, \quad (7.3)$$

$$\frac{d|A_1|}{dt} = \sigma_1 |A_1| + \beta_{H,2} |A_H| \cdot |A_2|, \quad (7.4)$$

$$\frac{d|A_2|}{dt} = \sigma_2 |A_2| + \beta_{H,1} |A_H| \cdot |A_1|, \quad (7.5)$$

where  $|A_F|$ ,  $|A_H|$ ,  $|A_1|$  and  $|A_2|$  refer to the magnitudes of the fundamental mode, its first harmonic, a perturbed mode 1 and a perturbed mode 2, respectively. The perturbed modes must satisfy resonance conditions, namely  $i_1 + i_2 = i_H$ . In (7.1), the quadratic terms are complex conjugates, whereas in (7.4) and (7.5) it was assumed for simplicity that the phases satisfy  $\phi_1 + \phi_2 = -\phi_H$  and cancel out.

Initially, mode 2 grows as  $\exp(\sigma_2 t)$ . When the amplitude of mode 2 is large enough, the quadratic terms will make the amplitude grow as  $\exp((\sigma_H + \sigma_1)t)$ . As  $\sigma_H + \sigma_1 \gg \sigma_2$ , at some point in time following the initial exponential growth of mode 2 we begin to see a rapid exponential growth.

For the general case with a Reynolds number ramp, in (7.2) to (7.5) we can replace the growth rates with linear functions as defined by (4.9). A similar argument for the region of rapid exponential growth can be applied where the log of the amplitude in this region now grows quadratically in time. We can assume that  $l_i$ ,  $\alpha_{ij}$  and  $\beta_{jq}$  do not vary with  $Re$ , although more numerical runs will be required to determine the degree to which this is valid. However, it is a reasonable assumption considering that the Reynolds number is assumed to be not far from the critical value.

In figure 3, for  $T = 50$  and  $T = 75$ , the preferred mode is mode 11. In these figures, during the ramp, the log of the amplitude of mode 12 varies quadratically with time whilst its amplitude is small, followed by a rapid acceleration prior to the saturation of mode 11. It is suggested that this is partly due to the first harmonic ( $i_H = 22$ ) of the fundamental mode ( $i_F = 11$ ) interacting simultaneously with the smaller-amplitude modes  $i_1 = 10$  and  $i_2 = 12$ , bringing about a mutual reinforcement or resonance of these two modes (since the condition under which the resonance occurs is satisfied). One also expects mutual reinforcements of modes  $i_1 = 9$  and  $i_2 = 13$ ,  $i_1 = 8$  and  $i_2 = 14$ , and so on. These resonances are a result of interactions with the first harmonic of mode 11. These are also manifested as rapid accelerations prior to the saturation of the fundamental mode.

In figure 3, for  $T = 100$  and  $T = 150$ , the preferred mode is mode 10. In these figures, the first harmonic ( $i_H = 20$ ) of the fundamental mode ( $i_F = 10$ ) interacts simultaneously with the smaller-amplitude modes  $i_1 = 11$  and  $i_2 = 9$ , bringing about a mutual reinforcement of these two modes. With respect to the first harmonic of mode 10, resonances are also expected for  $i_1 = 8$  and  $i_2 = 12$ ,  $i_1 = 7$  and  $i_2 = 13$ , and so on.

It is also noticed that the lower the amplitude of the unpreferred mode, the earlier it begins to accelerate. This feature is accounted for by the quadratic term in (7.5) if the lower amplitude mode is  $i_2$ .

Although we have discussed resonances with respect to interactions with the first harmonic of the preferred mode there are also contributions to the resonance due to interactions with the first harmonics of the other modes.

We can envisage an  $N$ -dimensional phase space spanned by  $\{|A_1|^2, |A_2|^2, \dots, |A_N|^2\}$ . Solving (2.6) for  $d|A_i|^2/dt = 0$  gives the coordinates of all the equilibrium points. When the coupling constants  $\alpha_{ij}$  satisfy some set of strong coupling conditions then we obtain  $N$  stable equilibrium points in the phase space. We can perceive the  $N$  stable equilibrium points as a model for a discrete set of  $N$  possible Taylor-vortex

flows within the Eckhaus stable band. The strong coupling conditions can themselves be viewed as conditions for non-uniqueness of the  $N$ -mode system. Assuming that the initial amplitudes of the modes are the same, the preferred state varies with ramp time.

## 8. Conclusions

A linear model was shown to describe the behaviour of the amplitude of the modes in their independent stage of growth. The total time for the amplitude of a mode to grow to high amplitudes, where nonlinear effects were important, was equal to the time it would take for impulsive increases plus a delay time. The delay time has a shortest-to-longest ordering of the modes corresponding to the lowest-to-highest ordering of the critical Reynolds number of each mode. As the time delay is proportional to the ramp time, progressively longer ramp times result in a change of the ordering of the time taken for each mode to begin self-interaction. Then, for a particular ramp time, the mode which has sufficient time to self-interact will become preferred. When the ramp time was sufficiently large, the delay time outweighed the time taken for impulsive increases. In this case, the amplitude of the mode with the critical wavelength was delayed the least from growing to high amplitudes, where the flow self-interacted and approached the form of a steady Taylor-vortex flow.

For the case examined in this paper, the model parameters for the linear model were determined and used to predict the selected wavelength of the Taylor-vortex flow. These analytical predictions agree with the observed final states from the numerical simulations.

The description of the mode selection is as follows. For short ramp times, the mode with the maximum growth rate at the final Reynolds number is selected since the Taylor vortices must grow and saturate effectively at this final Reynolds number. However, this relies on the modes having the same initial amplitude. For long ramp times, (4.14) reduces to (4.16), which gives the minimum  $t_\lambda^*$  for the critical wavelength. Physically, the critical mode has time to grow to significant amplitudes before the other modes begin to grow. This is true even if the critical mode is initially damped faster than some other mode. In particular, for increasingly long ramp times, the critical mode is preferentially selected independent of its initial amplitude. The linear model describes this process mathematically. Given the initial mode amplitudes and their growth rate coefficients (derived from numerical simulations or linear stability analysis) it is possible to predict the final state for any ramp time and the approximate time at which saturation begins to set in.

Finally, to take account of rapid growth of some modes prior to saturation, a nonlinear model has been suggested which includes three-way resonant mode interactions. This model can account for the observed features of the nonlinear behaviour. It may be possible to determine the model coefficients through careful numerical experiments in future work.

## REFERENCES

- ABARBANEL, D. D., RABINOVICH, M. I. & SUSHCHIK, M. M. 1993 *Introduction to Nonlinear Dynamics for Physicists*. World Scientific.
- ANDERECK, C. D. & BAXTER, G. W. 1988 An overview of flow regimes in a circular Couette system. In *Propagation in Systems far from Equilibrium* (ed. J. E. Wesfreid & H. R. Brand), pp. 315–324. Springer.
- ANDERECK, C. D., LIU, S. S. & SWINNEY, H. L. 1986 Flow regimes in a circular Couette system with independently rotating cylinders. *J. Fluid Mech.* **164**, 155–183.

- ANTONIOJAN, J. & SANCHEZ, J. 2002 On stable Taylor vortices above the transition to wavy vortices. *Phys. Fluids* **14**, 1661–1665.
- BURKHALTER, J. E. & KOSCHMIEDER, E. L. 1973 Steady supercritical Taylor-vortex flow. *J. Fluid Mech.* **58**, 547–560.
- BURKHALTER, J. E. & KOSCHMIEDER, E. L. 1974 Steady supercritical Taylor vortices after sudden starts. *Phys. Fluids* **17**, 1929–1935.
- CHANDRASEKHAR, S. 1961 *Hydrodynamic and Hydromagnetic Stability*. Oxford University Press.
- COLES, D. 1965 Transition in circular Couette flow. *J. Fluid Mech.* **21**, 385–425.
- DE ROQUEFORT, T. A. & GRILLARD, G. 1978 Computation of Taylor vortex flow by a transient implicit method. *Comput. Fluids* **6**, 259–269.
- DRAZIN, P. G. & REID, W. H. 1989 *Hydrodynamic Stability*. Cambridge University Press.
- EAGLES, P. M. 1971 On stability of Taylor vortices by fifth-order amplitude expansions. *J. Fluid Mech.* **49**, 529–550.
- HAIDVOGEL, D. B. & ZANG, T. 1979 Accurate solution of Poisson's equation by expansion in Chebyshev polynomials. *J. Comput. Phys.* **30**, 167–180.
- HOURIGAN, K., GRAHAM, L. & THOMPSON, M. C. 1998 Spiral streaklines in pre-vortex breakdown regions of axisymmetric swirling flows. *Phys. Fluids* **7**, 3126–3128.
- JONES, C. A. 1984 The transition to wavy Taylor vortices. *J. Fluid Mech.* **157**, 135–162.
- KARNIADAKIS, G. E., ISRAELI, M. & ORSZAG, S. A. 1991 High-order splitting methods for incompressible Navier–Stokes equations. *J. Comput. Phys.* **97**, 414–443.
- KOGELMAN, S. & DIPRIMA, R. C. 1970 Stability of spatially periodic supercritical flows in hydrodynamics. *Phys. Fluids*, **13**, 1–11.
- KOSCHMIEDER, E. L. 1993 *Bénard Cells and Taylor Vortices*. Cambridge University Press.
- LIM, T. T., CHEW, Y. T. & XIAO, Q. 1998 A new flow regime in Taylor–Couette flow. *Phys. Fluids* **10**, 3233–3235.
- LIU, D. C. S. & CHEN, C. F. 1973 Numerical experiments on time-dependent rotational Couette flow. *J. Fluid Mech.* **59**, 77–95.
- MARCUS, P. S. 1984 Simulation of Taylor–Couette flow. Part 1. Numerical methods and comparison with experiment. *J. Fluid Mech.* **146**, 45–64.
- NEITZEL, G. P. 1982 Stability of circular Couette flow with variable inner cylinder speed. *J. Fluid Mech.* **123**, 43–57.
- PARK, K., GERALD, L. & DONNELLY, R. J. 1981 Determination of transition in Couette flow in finite geometries. *Phys. Rev. Lett.* **47**, 1448.
- RIGOPOULOS, J. 1998 On numerical simulation of Taylor–Couette flow and state selection in Taylor-vortex flow. PhD thesis, Monash University, Melbourne, Australia.
- SNYDER, H. A. 1969 Wave-number selection at finite amplitude in rotating Couette flow. *J. Fluid Mech.* **35**, 273–298.
- TAYLOR, G. I. 1923 Stability of a viscous liquid contained between two rotating cylinders. *Phil. Trans. R. Soc. Lond. A* **223**, 289–343.
- THOMPSON, M. C., HOURIGAN, K. & SHERIDAN, J. 1996 Three-dimensional instabilities in the wake of a circular cylinder. *Expl Therm. Fluid Sci.* **12**, 190–196.
- XIAO, Q., LIM, T. T. & CHEW, Y. T. 2002 Second Taylor vortex flow: effects of radius ratio and aspect ratio. *Phys. Fluids* **14**, 1537–1539.